arXiv:1410.1887v1 [astro-ph.GA] 7 Oct 2014

Tidal stripping stellar substructures around four metal-poor globular clusters in the Galactic bulge

Sang-Hyun Chun[1], Minhee Kang[2], DooSeok Jung[2], Young-Jong Sohn[2]

Received _____; accepted _____

To be submitted to the Astronomical Journal

[1]Yonsei University Observatory, Seoul, Korea; shchun@galaxy.yonei.ac.kr

[2]Department of Astronomy, Yonsei University, Seoul 120-749, Korea

ABSTRACT

We investigate the spatial density configuration of stars around four metal-poor globular clusters (NGC 6266, NGC 6626, NGC 6642 and NGC 6723) in the Galactic bulge region using wide-field deep J, H, and K imaging data obtained with the WFCAM near-infrared array on United Kingdom Infrared Telescope. Statistical weighted filtering algorithm for the stars on the color-magnitude diagram is applied in order to sort cluster member candidates from the field star contamination. In two-dimensional isodensity contour maps of the clusters, we find that all of the four globular clusters exhibit strong evidence of tidally stripping stellar features beyond tidal radius, in the form of tidal tail or small density lobes/chunk. The orientations of the extended stellar substructures are likely to be associated with the effect of the dynamic interaction with the Galaxy and the cluster's space motion. The observed radial density profiles of the four globular clusters also describe the extended substructures; they depart from theoretical King and Wilson models and have an overdensity feature with a break in a slope of profile at the outer region of clusters. The observed results could imply that four globular clusters in the Galactic bulge region have experienced strong environmental effect such as tidal force or bulge/disk shock of the Galaxy in the dynamical evolution of the globular clusters. These observational results provide us further constraints to understand the evolution of clusters in the Galactic bulge region as well as the formation of the Galaxy.

Subject headings: Galaxy: bulge — Galaxy: structure — globular clusters: general — globular clusters: individual(NGC 6266, NGC 6626, NGC 6642, and NGC 6723)

1. INTRODUCTION

According to modern cold dark matter cosmology, galaxies are hierarchically assembled by the merging or accretion of small fragments (Baugh et al. 1996; Klypin et al. 1999; Moore et al. 1999; Diemand et al. 2007). In this theory, the stellar halo of galaxies, such as the Milky Way, are mostly built up from small substructures such as satellite galaxies (Searle & Zinn 1978; Johnston 1998; Bullock et al. 2001; Abadi et al. 2006; Font et al. 2006; Moore et al. 2006). These satellite systems suffer significant tidal disruption and mass loss by the tidal force and shock of host galaxies during the process of accretion, thereby producing a number of stellar substructures, such as tidal tails or streams in the galactic halo (Bullock & Johnston 2005). Thus, the study of stellar streams in the Milky Way is a valuable for reconstructing the accretion history of the Galaxy (Koposov et al. 2010; Law et al. 2009) and for understanding the potential of the Galaxy (Odenkirchen et al. 2009)

In the last two decades, numerous stellar streams and tidal tails have been discovered in the Galactic halo. The Sagittarius dwarf galaxy and its stellar streams (Ibata et al. 1994, 1995, 1997, 2001; Vivas et al. 2001; Majewski et al. 2003; Newberg et al. 2003; Martinez-Delgado et al. 2004; Belokurov et al. 2006a) are the most well studied out of the many other recently discovered stellar streams (Helmi et al. 1999; Ivezić et al. 2000; Yanny et al. 2000, 2003; Newberg et al. 2002; Martin et al. 2004; Rocha-Pinto et al. 2004; Martinez-Delgado et al. 2005; Duffau et al. 2006; Grillmair 2006; Jurić et al. 2008). Sky survey projects, such as the Sloan Digital Sky Survey (SDSS) and the Two Micron All Sky Survey (2MASS), are discovering more stellar substructures in the Galactic halo; newly-discovered stellar streams include the Virgo stellar stream (Vivas & Zinn 2006; Vivas et al. 2008), the Orphan Stream (Grillmair 2006; Zucker et al. 2006; Belokurov et al. 2007), and the Cetus stream (Newberg et al. 2009; Koposov et al. 2012). More recent works

have reported that some of these streams are associated with globular clusters (Drake et al. 2013; Grillmair et al. 2013).

Globular clusters have been one of the most investigated stellar systems. They have provided crucial information about the formation and evolutionary mechanisms of the Galaxy. However, recent photometric and spectroscopic studies are still amending the accepted the view of how the globular clusters formed and their contribution to the formation of the Milky Way. It appears that they are not just simple stellar populations, as was previously thought (Gratton et al. 2004; Carretta et al. 2009), and some of them, such as ω Centauri (Lee et al. 1999) and NGC 6656 (Lee et al. 2009), are even considered to be surviving remnants of the first building block that merged into the Milky Way. Several globular clusters in the Milky Way (about 27% of the Milky Way's globular clusters; Mackey & Gilmore 2004) could have formed via the accretion or merging of more complex systems. In addition, recent work suggests that globular clusters were $8 - 25$ times more massive than they are present when they first formed (Conroy et al. 2011; Schaerer & Charbonnel 2011). Thus, the stellar streams around globular clusters are important objects to study for understanding the merging or accretion history of the Milky Way and to gather information regarding the dynamical evolution of globular clusters. Indeed, the remarkable long tidal tail of Palomar 5 (Odenkirchen et al. 2001; Grillmair & Dionatos 2006a) and NGC 5466 (Belokurov et al. 2006b; Grillmair & Johnson 2006), as well as the presumed globular cluster stream GD-1 (Grillmair & Dionatos 2006b), are spectacular examples of globular cluster streams. The tidal bridge-like features and common envelope structures around M53 and NGC 5053 (Chun et al. 2010) are also particularly interesting, as they are the evidence of an accretion event of dwarf galaxies into the Milky Way. Slightly extended tidal substructures also appear in the vicinity of several globular clusters (Grillmair et al. 1995; Leon et al. 2000; Sohn et al. 2003).

Despite numerous discoveries of globular cluster streams, most of the globular cluster streams found to date have been in the Galactic outer halo. However, there are more than 40 globular clusters in the Galactic bulge region, and the origin of metal-poor globular clusters in the bulge region is still unclear. There have been a few studies of the stellar streams of the globular clusters in the bulge region. The stellar substructure around globular cluster NGC 6626 was the first discovery in the bulge region (Chun et al. 2012). In a hierarchical model, it can be seen that vigorous merging events of subclumps exist in the bulge region of galaxies like the Milky Way (Katz 1992; Baugh et al. 1996; Zoccali et al. 2006). These merging events then result in a wide metallicity distribution ($-1.5 \leq [Fe/H] < 0.5$; McWilliam & Rich 1994; Zoccali et al. 2003) of stars in the bulge region (Nakasato & Nomoto 2003). Terzan 5 is an example of a merging event in the bulge region in the past (Ferraro et al. 2009). Therefore, we can expect to discover extratidal substructures around some of the globular clusters in the bulge region.

In this study, we investigated the spatial density distribution of stars around four metal-poor globular clusters in the Galactic bulge region - NGC 6266, NGC 6626, NGC 6642, and NGC 6723. We assigned the bulge region as the area within 3 kpc from the Galactic center. Table 1 shows the basic parameters of the four globular clusters. In order to reduce the effect of high extinction toward the bulge, we used wide-field ($45' \times 45'$) near-infrared JHK photometric data obtained from the observation of the Wide Field Camera (WFCAM) array attached to the United Kingdom Infrared Telescope (UKIRT). Section 2 presents our observations, data reduction process, and photometric measurements. The statistical analysis and filtering technique used for member star selection are described in Section 3. In Section 4, we investigate two-dimensional stellar density maps and the radial profile of the clusters to trace the stellar density features. The discussion of our investigation is presented in Section 5. Lastly, we summarize the results and discussion in Section 6.

2. OBSERVATION, DATA REDUCTION AND PHOTOMETRY

Photometric imaging data for four globular clusters were observed using the WFCAM on the 3.8 m UKIRT in Hawaii in April and July of 2010. The WFCAM is an infrared mosaic detector of four Rockwell Hawaii-II (HgCdTe 2048×2048) arrays with $12'.83$ gap between the arrays. Four separately pointed observations (four tiles) result in a filled-in sky area of 0.75 square degrees with a pixel scale of $0'.4$. Our target clusters were observed using the four-tile observations in three band filters (J, H, and K) to get continuous sky images covering a total field-of-view of 0.75 square degrees. The individual image of each cluster for one tile was recorded in short (1 sec for JHK) and long (5 sec for JH, and 10 sec for K) exposures to optimize the photometry of bright and faint stars. A five-point dithering pattern was applied to reject bad pixels and cosmic rays. At each dithered position, 2×2 micro-stepping observation was also carried out to get well-sampled stars. A separate sky observation was obtained for removing thermal background emission after observing the target images. We also observed several comparison fields in the bulge region using the same observation strategy for observing the clusters. The stars in the comparison field area were used in the processes of color-magnitude (C-M) mask filtering technique and the optimal contrast filtering technique in the following section in order to estimate the field star contamination around the globular clusters on the color-magnitude diagram (see Section 3). Three comparison fields were finally selected using the following condition: the comparison field was not very distant from the clusters on the sky, and the morphology of the color-magnitude diagram for the field stars was similar to that of the globular clusters. The coordinates of the selected comparison fields were indicated in Table 1. Table 2 provides the exposure time of each filter for the four globular clusters.

Standard data reduction for near-infrared imaging, which includes dark subtraction, flat fielding, and the removal of crosstalk, was completed by the pipeline of the Cambridge

Astronomy Survey Unit (CASU). Then thermal emission backgrounds were made by median-combining the CASU-processed images of the separate sky observations. The resulting blank sky images were subtracted from the all target images. The residual sky background level of each target image was also removed in each target image. All sky-subtracted images were interleaved into a single image for photometric analysis using Swarp (Bertin et al. 2002). The final resampled images of the four globular clusters have a wide-field area of about $45' \times 45'$, which is sufficiently large area to cover from the center of each target cluster to two times its tidal radius. The average seeing condition of stars in the resampled images is between $0.75 \sim 1.05$ arcsec. Table 2 summarizes the average FWHM values for each filter.

Stellar photometry on each detector was performed using the point-spread function (PSF) fitting routine ALLSTAR (Stetson & Harris 1988). The PSF varying quadratically through position was first constructed with $100 - 150$ bright and isolated stars using the DAOPHOT II program (Stetson 1987). The quality of the PSF was improved by removing the neighboring faint stars around the PSF stars and iteratively reconstructing the PSF. Then, the instrumental magnitude of the individual stars on each array was estimated by the ALLSTAR process using improved PSF. The raw positions of the stars on the detector were transformed into an equatorial coordinated system using the Two Micron All Sky Survey (2MASS) point-source catalog. The instrumental magnitudes of the stars were transformed on to the 2MASS filter system using the color term between WFCAM and the 2MASS system (Dye et al. 2006). Then the photometric zero-points were finally computed and calibrated by comparing the magnitudes of common stars in our photometric catalog and 2MASS catalog. The astrometric and photometric data of each chip on a mosaic were finally combined into a whole set of data for the target cluster. Stellar objects with photometric measurement error larger than 0.1 mag were removed in order to reduce the spurious detection. We also measured the individual extinction value of each star according

the position of the sky by using the map of Schlegel et al. (1998); the mean E(J-K) and extinction values in K are $E(J-K) = 0.19$ and $A_K = 0.14$ for NGC 6266, $E(J-K) = 0.24$ and $A_K = 0.18$ for NGC 6626, $E(J-K) = 0.20$ and $A_K = 0.15$ for NGC 6642, and $E(J-K) = 0.12$ and $A_K = 0.08$ for NGC 6723. We subtracted derived extinction values from the observed magnitude.

3. PHOTOMETRIC FILTERING FOR MEMBER STAR SELECTION

In order to accurately trace the stellar distribution around the globular clusters, it is important to reduce the contamination of the field stars and to enhance the density contrast between the cluster candidate stars and the field stars. Although many statistical methods for filtering field stars have been introduced in the past few decades, the color-magnitude (C-M) mask filtering technique (Grillmair et al. 1995) and the optimal contrast filtering technique (Odenkirchen et al. 2003) were frequently used. We also basically followed these two methods (for a detailed description, see Grillmair et al. 1995; Odenkirchen et al. 2003; Chun et al. 2012).

We first define new orthogonal color indices c_1 and c_2 from the one-dimensional distribution of stars in a $(J-K)$ versus $(J-H)$ color-color diagram (see Figure 2 of Chun et al. 2012). The color indices were chosen in such a way that the c_1 axis was placed along the main distribution of the stars, while the c_2 axis was perpendicular to the c_1 axis. Equation 1 shows the general forms of two orthogonal color indices, and Table 3 indicates the coefficients a and b of the new color indices for each cluster.

$$c_1 = a(J-K) + b(J-H), \tag{1}$$
$$c_2 = -b(J-K) + a(J-H)$$

In the (c_2, K) color-magnitude diagram (CMD), we rejected all stars with $|c_2| > 2\sigma_{c_2}(K)$, where $\sigma_{c_2}(K)$ is the dispersion in c_2 for stars with magnitude K. The stars within $2 \sim 5r_h$ for each cluster were used when we defined the rejecting limit. The left panel of Figure 1 shows a (c_2, K) CMD for stars in $2 \sim 5r_h$ from the cluster center. The lines indicate our rejecting limit; we considered that stars outside this boundary were unlikely to be cluster member stars.

After this preselection in the (c_2, K) plane, we defined the locus of cluster on the CMD where the signal-to-noise ratio (S/N) of the cluster star count was maximized in contrast to the comparison field stars using the C-M mask filtering technique in the (c_1, K) plane. First, we made a representative sample of CMDs for the cluster and the fields using the stars in the central region of the cluster and the observed comparison fields. The second and third panels of Figure 1 show the (c_1, K) CMDs of stars within $3'.0 \sim 4'.0$ from each cluster center and the selected comparison region, respectively. The right panel shows the (c_1, K) CMD of the stars in the total survey region for the cluster. Then, the CMDs of the cluster and comparison were subdivided into small subgrid elements, and the signal-to-noise ratio in each subgrid element was calculated using Equation 2:

$$s(c_1, K) = \frac{n_{cl}(c_1, K) - g n_f(c_1, K)}{\sqrt{n_{cl}(c_1, K) + g^2 n_f(c_1, K)}}, \tag{2}$$

where $n_{cl}(c_1, K)$ and $n_f(c_1, K)$ are the number of stars in the subgrid elements for the cluster and comparison region, respectively; g is the area ratio of the cluster region to comparison region. From array s, we computed the cumulative number of stars for the cluster $N_{cl}(k)$ and comparison $N_f(k)$, respectively, by sorting the elements of $s(c_1, K_s)$ into a series of descending order with a one-dimensional index of k. Then, a cumulative signal-to-noise ratio $S(k)$ was calculated by Equation (3):

$$S(k) = \frac{N_{cl}(k) - g N_f(k)}{\sqrt{N_{cl}(k) + g^2 N_f(k)}} \tag{3}$$

$S(k)$ become a maximum value for a specific subarea of the C-M plane, and the $s(c_1, K)$ corresponding to the maximum value of $S(k)$ was chosen as an optimal threshold, s_{lim}. The filtering mask area in the (c_1, K) plane was then determined by selecting subgrid elements with larger $s(c_1, K)$ values than the determined s_{lim}. The solid lines in the second, third, and fourth panels in Figure 1 represent the selected filtering mask envelope. The entire sample of stars in the determined filtering mask area was considered in the following filtering analysis.

Finally, we applied the optimal contrast filtering technique to the stars in the determined filtering mask envelope obtained from the C-M mask filtering technique. We calculated the number density distribution of star in (c_1, K) C-M plane (Hess diagram) for cluster and comparison field. The bin size of the Hess diagram is the same as that of the C-M mask filtering technique. Then, the density of cluster stars $n_c(k)$ at a given position k on the sky was derived by Equation 4:

$$n_c(k) = \frac{\sum_j [n(k,j) f_c(j)/f_F(j) - n_F(k,j) f_c(j)/f_F(j)]}{\sum_j f_c^2(j)/f_F(j)}, \tag{4}$$

where $n_c(k,j)$ and $n_F(k,j)$ are cluster star density and field star density in the jth subgrid in the optimal mask envelope of the C-M plane and in the kth bin in position on the sky; f_c and f_F are the normalized density distribution of the cluster and comparison field in the optimal mask envelope in the Hess diagram of (c_1, K). In the optimal contrast filtering technique, the ratio $f_c(j)/f_F(j)$ of the number density distribution of the cluster stars to the comparison field stars in optimal mask envelope of (c_1, K) CMD was used as conditional weight to determine cluster membership. The number density of stars in the sky was calculated by summing up the conditional weights of all stars and dividing this sum by the factor $a = \sum_j f_c^2(j)/f_F(j)$. Thus, this returns the estimated number of cluster stars n_c plus a term of n_F/a, the number of contaminating field stars attenuated by a.

4. Spatial density features of stars in the vicinity of the four globular clusters

In this section, we present the spatial density features of the stars in the vicinity of the four globular clusters. The large area of the WFCAM data ($45' \times 45'$ of the sky) enable us to examine the features of the stellar density distribution from the cluster center to a distance of at least two times the tidal radius. The two-dimensional density distribution and the radial density profile for each cluster were investigated using the selected stars by C-M mask filtering technique and the weighted number obtained from the optimal contrast filtering technique.

The two-dimensional stellar surface density maps of the clusters were constructed using Equation 4. The sky plane of cluster was divided into small grids with pixel width of $0'.9 \times 0'.9$, and the weighted counts of stars were calculated in those pixels. The field stars contamination was then constructed by masking the central region within $1 \sim 1.5r_t$ and fitting a low-order bivariate polynomial model. Figure 2 shows the constructed field stars contamination for each cluster, and the density gradients or variations of field stars across the globular cluster were represented with gray scale. We subtracted these field stars contamination maps and made the field across the globular cluster essentially flat. The residual background density map was also made using the same method with field star contamination maps, but in this case, we just subtracted the mean density level of residual background density map. The star number density map of each cluster was then smoothed with a Gaussian smoothing algorithm to increase signal-to-noise ratio and enhance the spatial frequencies of interest. The isodensity level was described by contour with a standard deviation unit (σ) of the background level on the smoothed map with the various kernel values. The distribution map of the E(B-V) value for the observed region was also derived from the map of Schlegel et al. (1998) to examine possible extinction effects.

The radial number density profiles of the globular clusters are useful for understanding

the internal and outer structure of the globular clusters. This overall structure has been described for a long time by King (1966) model, which is characterized by a truncated density profile at the outer edge. However, according to the results of a recent wide-field observation, the radial number density profiles of several globular clusters are not truncated at their outer edges; instead, they have an extended overdensity feature that departs from the behavior predicted by King (1966) model and smoothly drops toward the background level (Grillmair et al. 1995; Leon et al. 2000; Testa et al. 2000; Rockosi et al. 2002; Lee et al. 2003; Olszewski et al. 2009; Carballo-Bello et al. 2012). Numerical simulations also reproduced and characterized this overdensity feature as a break in the slope of radial profile due to the extratidal stars around globular clusters (Combes et al. 1999; Johnston et al. 1999, 2002). In these models, the break in the slope of the radial profile was described by the power law $r^{-\gamma}$. Wilson (1975) models has also been used to describe the structure of globular clusters. Indeed, McLaughlin & van der Marel (2005) fitted Wilson model to the radial density structure of globular clusters in the Galaxy and the Magellanic Clouds. We note that Wilson model is spatially more extended than King model (see McLaughlin & van der Marel 2005).

We also derived the radial surface density profile of each cluster and tried to find the evidence of an extratidal extension at the outer edges of the clusters. In order to construct the radial density profiles, we used concentric annuli with a width of $0^{'}.45$ ranging from the cluster center out to a radius of $20^{'}.0$, and then counted the weighted number of stars in each annulus. The number density of stars was then calculated by dividing the sum by the area of the annulus. The field stars contribution on the radial profile was estimated from the field star contamination maps in Figure 2, and subtracted from the radial profile. Then the residual background density level which was measured on the residual background density map was also removed from the counts. The error on the number density was estimated by the error propagated from a Poisson statistic for star

counts. We examined the radial completeness for measuring the crowding effect of the inner regions of the clusters by applying the artificial star test and then recovered the crowding effect using the radial complete ratio. However, the most central regions of the clusters were not resolved enough to derive the number density profile because of the crowding effect even though we compensated for the number density. Therefore, for the central regions, we combined our number density profiles with the previously published surface brightness profiles of Trager et al. (1995). The surface brightness profile of Trager et al. (1995) was converted into a number density scale by the equation, $logN(r) = -\mu(r)/2.5 + C$, where C is an arbitrary constant to match the number density profile and surface brightness profile. Then, the final number density profiles were empirically fitted by King model and Wilson model. We also derived radial surface density profiles for a different direction, for which we divided an annulus into eight sections (S1-S8) with an angle of 45°, as shown in Figure 3. The annulus widths were assigned to be $\sim 0'.5$ at innermost region with $r < 5'$, $\sim 1'.0$ at the middle region with $5' < r < 10'$, and $2'.0$ at outer region with $10' < r < 20'$. We note that some radial density points with small number statistics could not be plotted because the number densities in these regions were lower than background density level.

4.1. NGC 6266 (M62)

The star count map around NGC 6266 and the surface density maps smoothed by a Gaussian kernel value of $0°.045$ and $0°.12$ are shown in Figure 4, from the top-left panel to the bottom-left panel. The grey density map in the bottom-right panel of Figure 4 is the distribution map of E(B-V) of Schlegel et al. (1998). The contour lines indicate $0.5\sigma, 1.0\sigma, 2.0\sigma, 3.0\sigma, 4.0\sigma, 6.0\sigma$ and 10.0σ. The contour lines with a Gaussian kernel value of $0°.12$ are overlaid in a star count map and the E(B-V) map. The direction toward the Galactic center and the perpendicular direction to the Galactic plane are indicated

as a solid line and dashed line, respectively. The proper motion of NGC 6266, i.e. $\mu_\alpha \cos\delta = -3.50 \pm 0.37$ mas yr^{-1} and $\mu_\delta = -0.82 \pm 0.37$mas yr^{-1} (Dinescu et al. 2003), is indicated by a long arrow. The circle in each panel is the tidal radius of $r_t = 8'.97$ (Harris 1996).

Figure 4 clearly shows overdensity substructures around NGC 6266 that extend toward east and north-west directions to $\sim 1.5r_t$ at levels larger than 0.5σ. The stellar substructure in the east direction lies along the direction of the Galactic center and the opposite direction of the proper motion. In addition, the extended structure to the north-west is likely aligned with the opposite perpendicular direction to the Galactic plane, and its marginal extension seems to bend to the direction of proper motion. We note that the density feature at the southern region of the cluster is likely to be affected by the dust extinction as shown in bottom-right panel of Figure 4.

In the upper panel of Figure 5, the radial surface density profile of NGC 6266 is plotted, along with King model and Wilson model, which are arbitrarily normalized to our measurements. In the central region of the cluster, we replaced the number density profile with the surface brightness of Trager et al. (1995). The profile of Trager et al. (1995) connects smoothly with our number density profile at a radius of $log(r') \sim 0.4$. However, the number density profile shows an overdensity feature which departs from the King model and profile of Trager et al. (1995), with a break in the slope at the radius of $\log(r')\sim 0.65$ ($\sim 0.5r_t$). Here, we note that the profile of Trager et al. (1995) in the outer region might suffer from the background contamination and biases of bright stars (see Chun et al. 2012; Noyola & Gebhardt 2006), while our number density profile in this study has no bias due to bright stars. The overdensity feature seems to extend to the radius of $\log(r')\sim 1.15$ ($\sim 1.5r_t$). Wilson model shows a more extended profile to the outer region and seems to fit better with our measurements than the King model. The excess density at

this radial distance resembles a radial power law with a slope of $\gamma = -2.90 \pm 0.19$, which is steeper than the case of $\gamma = -1$, predicted for a constant mass-loss rate over a long time (Johnston et al. 1999). Thus, the overdensity feature at the outer region of NGC 6266 is indeed evidence of the extended substructures shown in Figure 4.

The lower panel of Figure 5 shows the radial surface number density profiles for eight angular sections with a different direction as shown in Figure 3. We note that the some radial density points in section 5,6,7, and 8 were not presented because the number densities in these region were lower than subtracted residual background level. The radial profiles in sections 1,2,3, and 4 show the overdensity features at the radius of $0.5r_t \lesssim r \lesssim 1.5r_t$. The overdensity features in sections 1,3 and 4 seem to extend to more distant radius than $1.5r_t$. The mean surface densities (μ) in these sections are particularly higher than the total average density and those in the other sections. In addition, the slope of profile in the sections 1 and 4 are shallower than the mean slope of profile and those of other angular sections. These mean density levels and shallow slopes in these sections are in good agreement with the extended stellar substructures in the direction of the Galactic center, in the opposite direction of the proper motion, and in the opposite perpendicular direction to the Galactic plane. On the other hand, the overdensity features do not appear in section 5,6, and 7 where prominent stellar substructures were not shown in two-dimensional contour map. The mean densities without overdensity features were also somewhat lower than total average density.

4.2. NGC 6626 (M28)

The top-left to bottom-right panels of Figure 6 show the star count map of NGC 6626, the isodensity contour map smoothed by a Gaussian kernel value of $0^\circ.045$ and $0^\circ.12$, and the distribution of E(B-V) extinction value of Schlegel et al. (1998). The isodensity contour

lines correspond to the level of $1.0\sigma, 1.5\sigma, 2.0\sigma, 3.0\sigma, 4.0\sigma$, and 6.0σ. The proper motion of $\mu_\alpha \cos\delta = 0.63 \pm 0.67$ mas yr^{-1} and $\mu_\delta = -8.46 \pm 0.67$ mas yr^{-1} (Casetti-Dinescu et al. 2013) is represented by a long arrow. The dashed line and solid line indicate the direction of the Galactic center and the perpendicular direction of the Galactic plane, respectively. The tidal radius of NGC 6626 (i.e., $r_t = 11'.27$) from Harris (1996) is also plotted as a circle.

In Figure 6, it is apparent that the stellar density distribution around NGC 6626 shows distorted overdensity features and extended tidal tails beyond the tidal radius. The tidal tails seem to stretch out symmetrically to both sides of the cluster, extending toward east and west directions from the cluster center to the radial distance of $\sim 2r_t$. In addition, the two tidal tails are likely to be aligned with the directions of the Galactic center and anti-center. Although there is no apparent extending features toward the direction of the proper motion in the surface density maps, there is a clumpy substructure in the northern area, which is aligned with the opposite direction of proper motion. Chun et al. (2012) first found the prominent overdensity feature that extends toward the perpendicular direction to the Galactic plane within the tidal radius of NGC 6626. We also found a stellar substructure similar to that found by Chun et al. (2012) in the contour map with a kernel values of $0°.045$. This substructure extends toward north-west direction within the tidal radius but is not as prominent as the substructure observed by Chun et al. (2012). We note here that our spatial density distribution has a wider field of view than that of Chun et al. (2012), which has enabled us to estimate and calibrate the underlying background substructure more accurately. Thus, the stellar density structure in this study is more homogeneous and less affected by field star contamination.

A radial surface density profile for NGC 6626 was presented in the upper panel of Figure 7. In the central region of the cluster, the number density profile was substituted with the surface brightness profile of Trager et al. (1995), which connects to the number

density profile at the middle range. The theoretical King model and Wilson model were also plotted to characterize the observed radial profile. It is apparent that our number density profile does not trace the King model and Wilson model at the outer region of the cluster; instead, it shows overdensity feature with a break in the slope of profile at the radius of $\log(r')\sim 0.5$ ($\sim 0.28r_t$). The overdensity feature extends out to the $\log(r')\sim 1.1$ ($\sim 1.5r_t$), and the profile in this region is characterized by a power law with a slope of $\gamma = -1.29 \pm 0.08$. This slope is not very different from the slope of $\gamma = -1$, predicted for a constant mass-loss rate over a long time (Johnston et al. 1999). The overdensity feature in the radial profile is indicative of extended tidal tails and substructures shown in Figure 6.

The radial surface density profiles of eight angular sections for NGC 6626 are plotted in the lower panel of Figure 7. In general, all the radial profile show the overdensity features with a break in slope at the outer region of the cluster. The estimated mean surface densities (μ) in angular sections 4,5 and 6 are higher than those in the other sections, and the slopes γ of profiles in section 4 and 5 are somewhat shallower than those in the other sections. Furthermore, the radial profiles in section 4 and 5 still maintain the overdensity features at the radial distance of $\log(r')\sim 1.3$. These overdensity features correspond to the apparent extratidal tails extending toward the direction perpendicular to the Galactic plane and direction of the Galactic center, as shown in Figure 6. Although the density in section 1 is not as high as that of section 5, this is because that the density near the tidal radius is low. Indeed, the weak connection between the cluster and tails is shown in contour map with a low kernal value of $0^\circ.045$. However, the tail extends out to a radial distance of $2r_t$, and this density feature is represented by a shallow slope in the and high density at the outer radius in radial profile of section 1.

4.3. NGC 6642

We plot star count map, isodensity contour maps, and the distribution map of E(B-V) value (Schlegel et al. 1998) from the top-left to bottom-right panel in Figure 8 in order to investigate of stellar distribution of NGC 6642. Gaussian kernel widths of 0°.045, and 0°.12 were applied to find spatial coherence in the stellar distribution. The isodensity contour levels are $0.5\sigma, 1.0\sigma, 2.0\sigma, 3.0\sigma, 5.0\sigma, 8.0\sigma$, and 10.0σ. The contour lines in the star count map and the distribution map of E(B-V) correspond to those of a smoothed map with a Gaussian kernel width of 0°.12. The circle centered on the cluster indicates the tidal radius of $r_t = 10.07'$ (Harris 1996). The solid and dashed lines represent the direction of the Galactic center and a perpendicular direction to the Galactic plane, respectively.

As can be seen in Figure 8, the stellar distribution of NGC 6642 seems to show a drop in density around the tidal radius in the specific direction, and clumpy structures outside of tidal radius. However, the prominent extended stellar substructure elongates in a northern direction beyond the tidal radius. A clumpy chunk in the southern region seems to be a counterpart to the overdensity feature in the northern region. A marginal extension also appears in an eastern direction, which seems to be aligned with the opposite perpendicular direction to the Galactic plane. Unfortunately, we could not find substructures that might be associated with the proper motion of the cluster, because the proper motion of NGC 6642 has not yet been reported.

The upper panel of Figure 9 shows the radial surface density profile of NGC 6642 along with the King model, the Wilson model and surface brightness profile of Trager et al. (1995). The radial surface profile of NGC 6642 shows apparent overdensity feature that depart from both model predictions from the radius of $\log(r')\sim 0.5$ ($\sim 0.3r_t$) to the tidal radius. However, the overdensity feature does not continue, and the density of radial profile decreases abruptly at the tidal radius. The drop in density and local clumpy substructures

around/outside tidal radius shown in Figure 8 seem to be associated with this fall of the radial profile and low density feature at the outer region. The overdensity feature within tidal radius was fitted by a power law with a slope $\gamma = -1.27 \pm 0.10$.

The radial surface density profiles for eight angular sections, which are plotted in the lower panel of Figure 9, represent better the stellar density distribution around NGC 6642 than average radial density profile in the upper panel of Figure 9. The radial profiles in angular sections 1 and 8 show clear overdensity features within tidal radius, and section 1 has the largest mean density of the eight sections. Although some radial points in these sections are not plotted because of small number statistics, there are still considerable number densities at the outer region. This is in agreement with the overdensity feature extending toward the eastern side on the two-dimensional surface density map. In contrast to these angular sections, the overdensity feature in section 2 is disconnected at the tidal radius because of its low density at the outer region. In the two dimensional surface contour map, we can not find obvious stellar substructures in that region. The radial density profile in section 3 shows the most prominent overdensity features with high density and the flattest slope, and contains the density excess at the outer radius. These are representative of a prominent extending substructure in northern region on the isodensity contour map in Figure 8. In the section 7, the radial density profile is likely to show the overdensity feature associated with the counterpart of the extended substructure in the northern region. In the sections 4 and 5, we could not find clear overdensity feature, and two-dimensional contour map does not also show prominent stellar substructures in those regions.

4.4. NGC 6723

Figure 10 shows a star count map around NGC 6723, surface density maps smoothed with Gaussian kernel values of 0°.07 and 0°.11 and a distribution map of E(B-V)

value (Schlegel et al. 1998) from the upper-left panel to the lower-right panel. We note that different Gaussian kernel values for NGC 6723 were selected in order to highlight the structures with similar spatial extents. Isodensity contours were overlaid on the maps with contour levels of $2.0\sigma, 2.5\sigma, 3.0\sigma, 4.0\sigma, 5.0\sigma$, and 7.0σ. The long dashed line and solid line indicate the perpendicular direction to the Galactic plane and the direction of the Galactic center, respectively. The proper motion of NGC 6723, i.e., $\mu_\alpha \cos\delta = -0.17 \pm 0.45$ mas yr^{-1} and $\mu_\delta = -2.16 \pm 0.50$ mas yr^{-1} (Dinescu et al. 2003), was indicated with an arrow. The tidal radius of $r_t = 10'.51$ (Harris 1996) was represented by circle.

As can be seen in Figure 10, there are weak extended substructures beyond the tidal radius of NGC 6723 at levels larger than σ. Small density lobes are likely to extend toward the eastern and western sides; the direction of the Galactic center, perpendicular direction to the Galactic plane or their opposite directions. In addition, the isodensity contour lines show a horn-shaped structure in the northern region, which corresponds to the opposite direction of the proper motion. The marginal extension appears near the tidal radius in the southern region, but this weak substructure does not seem to be outgrowing anymore. We note that there is a huge reflection nebula in the distant souther region of the cluster. Thus dust in the outskirts of reflection nebula in the southern region could affect the detected number density of marginal extension in the southern region. Indeed, the value of $E(B-V)$ in the southeast region is higher than the values of other regions. Thus, there is a possibility that more extended stellar substructures could exist in the obscured region.

The radial surface densities for NGC 6723, measured in each concentric annulus, are shown in the upper panel of Figure 11. The theoretical King model and Wilson model were arbitrarily normalized to our measurements, and the surface brightness profile of Trager et al. (1995) was used as a substitute for our measurements in the central region. Apparently, the radial number density profile departs from the theoretical King model at

the outer region of the cluster, while Wilson model has a slightly better fit to our radial profile of the cluster. The overdensity feature, which departs from the King model with a break in slope, is shown at the radius of $\log(r')\sim0.8$ ($\sim0.6r_t$), and extends to the radius of $\log(r')\sim1.15$ ($\sim1.5r_t$). The slope in this overdensity region is characterized by a power law with a slope of $\gamma = -1.89 \pm 0.28$, which is steeper than the value predicted from a theoretical simulation with a constant orbit-averaged mass-loss rate (Johnston et al. 1999).

The radial surface profiles of eight angular sections are also shown in the lower panel of Figure 11. The overdensity feature in the region of $0.6r_t \lesssim r \lesssim 1.5r_t$ is commonly detected in specific angular sections. The radial profile in section 1, where the prominent substructure appears in the two-dimensional contour map, has the highest mean number density out of all the profiles of the eight sections. In addition, the densities in section 2, 5, and 8 have somewhat higher density levels in the overdensity region, which is in good agreement with the horn-shaped substructure, the side lobe in the west side, and the marginal structure in the south region shown in the Figure 10. Some radial points near tidal radius in section 7 were not plotted, because of its low number density. This low density feature also appears as a bay-shaped structure with low level contours in the southern region on the contour map with a kernel value of $0^\circ.07$. The possible narrow dust lane, which might extend from the reflection nebular in southern region, can cause this low number density feature. Unfortunately, the extinction map of (Schlegel et al. 1998) does not show an apparent dust lane because of its low resolution. Thus, the study of dust extinction with high resolution is necessary in order to study stellar distribution around the cluster.

5. DISCUSSION

All of our target clusters reside within ~ 3 kpc from the Galactic center. The ancient globular clusters in the inner region can provide clues regarding the formation of the Galactic bulge and disk. Indeed, the spatial, chemical and kinematical properties of several globular clusters in the inner regions are consistent with those of bulge, disk and even bar membership (Burkert & Smith 1997; Barbuy et al. 1998; Côté 1999; Heitsch & Richtler 1999). However, the definite decomposition of globular clusters between the bulge and disk or bar components is not a trivial task in the central region of the Galaxy because the inner regions of the Galaxy are superimposed by various stellar populations of bulge, disk, and bar. In addition, in the inner region of the Galaxy, the globular clusters experience extreme dynamical evolution due to bulge/disk shock and strong tidal effects (Aguilar et al. 1988; Shin et al. 2008). Thus, reliable measurements of metallicities, orbits, and distances for globular clusters in the central regions are necessary in order to understand the evolution of the globular cluster in the bulge region. In this section, we investigated the previous results of our target globular clusters, and discuss the properties of clusters that could affect the substructures around the globular clusters.

NGC 6266 is a high-density ($\log\rho_c \sim 5.34$; Jacoby et al. 2002; Possenti et al. 2003) and the ninth most luminous globular cluster located ~ 1.7 kpc from the Galactic center (Harris 1996). Dinescu et al. (2003) found that NGC 6266 has a large rotation velocity, suggesting that this cluster belongs to a disk system rather than to a pressure-supported system. The total destruction rate of this cluster is about $\nu_{tot} = 0.644$ per Hubble time, and destruction rate ratio is $\nu_{tot}/\nu_{evap} = 1.0$ (Gnedin & Ostriker 1997), where ν_{evap} is evaporation rate per Hubble time. These destruction rate and ratio indicate that the main process of dynamical evolution for this cluster is internally driven, such as two-body relaxation. In this study, we found that apparent marginal extensions around the cluster bent to the direction of

proper motion and were likely to show S-shaped features. Thus, we can interpret this orientation of stellar substructure as the signature that the evaporated stars by internal two-body relaxation are finding themselves in a Galactic orbit similar to that of the parent cluster. However, we also found that the stellar density configuration around NGC 6266 shows a spatial coherence associated with the effect of dynamical interaction with the Galaxy. The prominent density feature extended toward the direction of the Galactic center. Thus, our stellar density distribution around NGC 6266 could be interpreted as an example of dynamical cluster evolution that tidal shocking accelerates two-body relaxation (Kundic & Ostriker 1995; Dinescu et al. 1999). Lee et al. (2007) classified NGC 6266 as an extended blue horizontal branch (EHB) cluster, and also suggested that the clusters with EHB could be a remnant of the first building blocks in the early universe. Thus, the stellar density feature around NGC 6266 would be tidally associated with these unknown first building blocks. More accurate orbit information and an investigation of the field stars contamination around NGC 6266 are necessary to understand the dynamical evolution of NGC 6266.

NGC 6626 is massive and moderately metal-poor globular cluster in the Galactic bulge region. Dinescu et al. (1999) first found the thick-disk orbit for this cluster and then proposed the possibility that this cluster had been produced in a satellite galaxy and then departed from its parent during the accretion process. In addition, according to Lee et al. (2007), this cluster is moderate EHB cluster and could be a remnant of first building blocks. Chun et al. (2012) first found the stellar density substructure around NGC 6626, which extends toward the direction perpendicular to the Galactic plane, indicating a disk-shock effect. They also discussed the possibility of the accretion scenario for the origin of this cluster. More recently, Casetti-Dinescu et al. (2013) updated the proper motion and orbit of this cluster. They noted that the cluster is located at the apocenter and that its orbit is rather eccentric and disruptive, indicating that the cluster may experience substantial

mass loss. In our study, we did find prominent stellar substructures extending toward the Galactic center and anti-center directions. This spatial orientation of the tidal tails is in good agreement with the findings of Montuori et al. (2007); namely, that the inner tails are oriented toward the Galactic center direction in the apocenter position. Moreover, we confirmed the stellar substructure extending toward the perpendicular direction to the Galactic plane, which was found by Chun et al. (2012). Casetti-Dinescu et al. (2013) mentioned that their newly updated proper motion vector with the Solar motion subtracted is aligned with this substructure. They then speculated that the recent disk plane crossing about 4 Myr ago might have contributed to the construction of tidal extension in the perpendicular direction to the Galactic plane. Therefore, this cluster is very likely to suffer from the disk/bulge shock and the Galactic tidal force. However, the total destruction rate of $\nu_{tot} = 0.546$ per Hubble time and destruction ratio of $\nu_{tot}/\nu_{evap} \sim 1.0$ by Gnedin & Ostriker (1997) do not seem to be in agreement with our interpretation. Thus, we here note that recalculation of the destruction rate is necessary using recently updated proper motion and eccentric orbit.

NGC 6642 has dense central core with a high concentration $c = 1.99$ (Harris 1996). Previous studies (Trager et al. 1995; Balbinot et al. 2009) have also indicated that there is not a well-resolved core in the radial profile and have classified the cluster as core-collapsed cluster. Barbuy et al. (2006) noted that the age of NGC 6642 is comparable to that of M5 and then suggested that the cluster is one of the few genuine metal-poor and old clusters in the bulge region. Therefore it can contain fossil information about the Galaxy. On the other hand, Balbinot et al. (2009) examined the position of NGC 6642 in the HB type versus the metallicity diagram and found that NGC 6642 lies on the position of young halo populations, not on the position of old halo and disc/bulge populations. They concluded that NGC 6626 is a transition cluster between the inner halo and outer bulge, considering its age, its position in the Galaxy, and its HB morphology. They also found clear evidence

for the mass segregation and depletion of low-luminosity stars in the luminosity and mass function and attributed this dynamical structure to the disk and bulge shocking. Indeed, we did find clumpy stellar substructures which extend toward north direction and the opposite direction perpendicular to the Galactic plane beyond the tidal radius. The large total destruction rate of $\nu_{tot} = 1.90$ per Hubble time and destruction ratio of $\nu_{tot}/\nu_{evap} \sim 8.3$ by Gnedin & Ostriker (1997) also indicate that a strong environmental force, such as a tidal effect due to disk and bulge shocking, might affect the dynamical evolution of this cluster. Thus, we interpret that although NGC 6642 is a core-collapse cluster and two-body relaxation would affect the dynamical evolution of the cluster, the extended stellar substructures around NGC 6642 would be the result of a strong gravitational interaction with the Galaxy. Unfortunately, we were unable to investigate a definite association between the observed stellar substructure and the cluster's motion because there is no published proper motion information for this cluster. If we could obtain accurate proper motion for this cluster, we would be able to understand the dynamical evolution of the cluster and figure out the origin of the cluster; e.g., whether this cluster is a genuine metal-poor and old cluster in the bulge region or a transition cluster between the inner halo region and the outer bulge region.

NGC 6723, which has a relatively low concentration of density ($c = 1.05$, Harris 1996) and a moderate EHB morphology (Lee et al. 2007), is an old globular clusters in the Galactic bulge region. Although it has long been considered one of the genuine Galactic bulge globular clusters, the origin of the cluster is not obvious because there have only been few studies on this cluster. van den Bergh (1993) suggested that NGC 6723 would have a circular orbit motion in the central region of the Galaxy. However, Dinescu et al. (2003) measured the proper motion of the cluster and found that its orbit is highly inclined. Based on its kinematics and low metallicity, they concluded that NGC 6723 is a member of the halo system. Recently, Lee et al. (2007) suggested a different origin scenario that

metal-poor EHB globular clusters such as NGC 6723 would be relics of the first building blocks. The total destruction rate of $\nu_{tot} = 0.321$ per Hubble time and a rather high destruction ratio of $\nu_{tot}/\nu_{evap} \sim 2.0$ by Gnedin & Ostriker (1997) indicate that there would be weak tidal substructures around this cluster. Indeed, in our study we have found the tidal stripping features that are likely to be associated with the interaction with the Galaxy. The weak stellar density lobes, which extend toward the directions of the Galactic center and anti-center, were detected in the surface iso-density map. In addition, a marginal extension tracing the opposite direction of the proper motion was also detected. However, we could not exclude dust extinction effect on the stellar density distribution map. The thin dust lane of reflection nebula in the southern region of the cluster might hide the stellar extensions.

6. Summary

In this study, we investigated the stellar spatial density distribution around four metal-poor globular clusters (NGC 6266, NGC 6626, NGC 6642, and NGC 6723) in the Galactic bulge region using wide-field ($45' \times 45'$) near-infrared J, H, and K images obtained with the WFCAM camera on the UKIRT. In order to discard the field stars contamination and enhance density contrast between cluster member and field stars, we used the C-M mask filtering technique and the optimal contrast filtering technique on the cluster CMDs. Two-dimensional density contour maps of the clusters were examined, and radial density profiles were also investigated with King and Wilson models.

The two-dimensional stellar density contour maps for the four globular clusters showed asymmetric and extended features of the stars around the globular clusters. In particularly, three globular clusters (NGC 6266, NGC 6626, and NGC 6642) showed tidal extension and a stellar chunk beyond the tidal radius, while NGC 6723 showed weak density lobes near

the tidal radius. Such extended stellar substructures were aligned with the direction of the Galactic center and anti-center, the perpendicular direction to the Galactic plane or the direction of the cluster orbit motion. Thus, it is highly probably that target clusters are affected by the dynamical environment effect such as a tidal force and bulge/disk shock. The radial profile also represented the extended substructures in the two-dimensional contour maps as overdensity features with break in a slope. Although the observed radial profiles of clusters departed from the King and Wilson model at the outer region of cluster, Wilson model appeared to have a better fit with the observed radial density profile for the cluster, which seemed to experience less of an dynamical environment effect (e.g. NGC 6266 and NGC 6723).

We here note that internal driven such as two-body relaxations, also affects the extended stellar substructure around the globular clusters. The stellar extensions around NGC 6266 show a good example of internal driven. In this cluster, the stars might be primarily evaporated by two-body relaxation, and then be affected by environmental tidal force of the Galaxy. For other clusters, it is obvious that the two-body relaxation contributes to the extended stellar substructures around clusters. In contrast to the case of NGC 6266, however, the environmental effects such as tidal force of the Galaxy and bulge/disk shock would be main factors for the extended stellar substructures, even though the cluster such as NGC 6642 had very active two-body relaxations. In addition, a more accurate proper motion and orbit that is calculated using an accurate galaxy potential model could increase the portion of external effect on the dynamical evolution of the globular clusters in the bulge region. Indeed, although the tidal-shock rate of NGC 6626 was not comparable or larger than two-body relaxation rates in previous studies (Gnedin & Ostriker 1997; Dinescu et al. 1999), the orbit of NGC 6626, which was derived using more accurate proper motion and an axisymmetric and barred model of the Galaxy (Casetti-Dinescu et al. 2013), was found to be eccentric and more disruptive. Therefore, further studies of the dynamical

evolution of the globular clusters in the bulge region with accurate proper motion and a galaxy model are required to provide theoretical constraints of the configuration of stars around the globular clusters. In addition, further deep and wide-field photometric data for metal-poor and metal-rich globular clusters in the Galactic bulge could provide more accurate information about the dynamical evolution of globular clusters, thereby leading to an increased understanding of the origin of globular clusters in the bulge region, as well as the formation of the bulge region.

We are grateful to an anonymous referee for detailed comments that greatly improved this paper. This research was supported by the Basic Science Research Program through the National Research Foundation of Korea (NRF) funded by the Ministry of Education, Science and Technology (2013R1A1A2006826). This work is grateful for partial support from KASI-Yonsei DRC program of Korea Research Council of Fundamental Science and Technology (DRC-12-2-KASI).

REFERENCES

Abadi, M. G., Navarro, J. F., & Steinmetz, M. 2006, MNRAS, 365, 747

Aguilar, L., Hut, P., & Ostriker, J. P. 1988, ApJ, 335, 720

Balbinot, E., Santiago, B. X., Bica, E., & Bonatto, C. 2009, MNRAS, 396, 1596

Baugh, C. M., Cole, S., & Frenk, C. S. 1996, MNRAS, 283, 1361

Barbuy, B., Bica, E., & Ortolani, S. 1998, A&A, 333, 117

Barbuy, B., Bica, E., Ortolani, S., & Bonatto, C. 2006, A&A, 449, 1019

Bellazzini, M., Ferraro, F. R., & Ibata, R. 2003, AJ, 125, 188

Belokurov, V., Zucker, D. B., Evans, N. W., et al. 2006a, ApJ, 642, L137

Belokurov, V., Evans, N. W., Irwin, M. J., Hewett P. C., & Wilkinson, M. I. 2006b, ApJ, 637, L29

Belokurov, V., Evans, N. W., Irwin, M. J., et al. 2007, ApJ, 658, 337

Bertin, E., Mellier, Y., Radovich, M., Missonnier, G., Didelon, P., & Morin, B. 2002, in ASP Conf. Proc., Vol. 281, Astronomical Data Analysis Software and Systems XI, ed. D. A. Bohlender, D. Durand, & T. H. Handley (San Francisco, CA: ASP), 228

Bullock, J. S., & Johnston, K. V. 2005, ApJ, 635, 931

Bullock, J. S., Kratsov, A. V., & Weinberg, D. H. 2001, ApJ, 548, 33

Burkert, A., & Smith, G. H. 1997, ApJ, 474, L15

Casetti-Dinescu, D. I., Girard, T. M., Jílková, L., et al. 2013, AJ, 146, 33

Carballo-Bello, J. A., Gieles, M., Sollima, A., et al. 2012, MNRAS, 419, 14

Carretta, E., Bragaglia, A., Gratton, R., D'Orazi, V., & Lucatello, S. 2009, A&A, 508, 695

Chun, S.-H., Kim, J.-W., Kim, M. J., et al. 2012, AJ, 144, 26

Chun, S.-H., Kim, J.-W., Sohn, S. T., et al. 2010, AJ, 139, 606

Combes, F., Leon, S., & Meylan, G. 1999, A&A, 352, 149

Conroy, C., Loeb, A., & Spergel, D. N. 2011, ApJ, 741, 72

Côté, P. 1999, AJ, 118, 406

Diemand, J., Kuhlen, M., & Madau, P. 2007, ApJ, 667, 859

Dinescu, D. I., Girard, T. M., van Altena, W. F., & López, C. E. 2003, AJ, 125, 1373

Dinescu, D. I., Girard, T. M., & van Altena, W. F. 1999, AJ, 117, 1792

Drake, A. J., Catelan, M., Djorgovski, S. G., et al. 2013, ApJ, 765, 154

Duffau, S., Zinn, R., Vivas, A. K., et al. 2006, ApJ, 636, L97

Dye, S., Warren, S. J., Hambly, N. C., et al. 2006, MNRAS, 372, 1227

Ferraro, F. R., Dalessandro, E., Mucciarelli, A., et al. 2009, Nature, 462, 483

Font, A. S., Johnston, K. V., Bullock, J. S., & Robertson, B. E. 2006, ApJ, 638, 585

Gnedin, O. Y., & Ostriker, J. P. 1997, ApJ, 474, 223

Gratton, R., Sneden, C., & Carretta, E. 2004, ARA&A, 42, 385

Grillmair, C. J., Cutri, R., Masci, F. J., et al. 2013, ApJ, 769, L23

Grillmair, C. J. 2006, ApJ, 645, L37

Grillmair, C. J., & Dionatos, O. 2006a, ApJ, 641, L37

Grillmair, C. J., & Dionatos, O. 2006b, ApJ, 643, L17

Grillmair, C. J., Freeman, K. C., Irwin, M., & Quinn, P. J. 1995, AJ, 109, 2553

Grillmair, C. J., & Johnson, R. 2006, ApJ, 639, 17

Harris, W. E. 1996, AJ, 112, 1487

Heitsch, F., & Richtler, T. 1999, A&A, 347, 455

Helmi, A., White, S. D. M., de Zeeuw, P. T., & Zhao, H. 1999, Nature, 402, 53

Ibata, R. A., Gilmore, G., & Irwin, M. J. 1994, Nature, 370, 194

Ibata, R. A., Gilmore, G., & Irwin, M. J. 1995, MNRAS, 277, 781

Ibata, R., Irwin, M., Lewis, G., Ferguson, A. M. N., & Tanvir, N. 2001, Nature, 412, 49

Ibata, R. A., Wyse, R. F. G., Gilmore, G., Irwin, M. J., & Suntzeff, N. B. 1997, AJ, 113, 634

Ivezić , Ž., Goldston J., Finlator K., et al. 2000, AJ, 120, 963

Jacoby, B. A., Chandler, A. M., Backer, D. C., Anderson, S. B., & Kulkarni, S. R. 2002, IAU Circ., 7783, 1

Johnston, K. V. 1998, ApJ, 495, 297

Johnston, K. V., Choi, P. I., & Guhathakurta, P. 2002, AJ, 124, 127

Johnston, K. V., Sigurdsson, S., & Hernquist, L. 1999, MNRAS, 302, 771

Jurić, M., Ivezić , Ž., Brooks, A., et al. 2008, ApJ, 673, 864

Katz, N. 1992, ApJ, 391, 502

King, I. R. 1966, AJ, 71, 64 MNRAS, 400, 2162

Klypin, A., Kravtsov, A. V., Valenzuela, O., & Prada, F. 1999, ApJ, 522, 82

Koposov, S. E., Belokurov, V., Evans, N. W., et al. 2012, ApJ, 750, 80

Koposov, S. E., Rix, H.-W., & Hogg, D. W. 2010, ApJ, 712, 260

Kundic, T., & Ostriker, J. P. 1995, ApJ, 438, 702

Law, D. R., Majewski, S. R., & Johnston, K. V. 2009, ApJ, 703, L67

Lee, J.-W., Kang, Y.-W., Lee, J., & Lee, Y.-W. 2009, Nature, 462, 480

Lee, K. H., Lee, H. M., Fahlman, G. G., & Lee, M. G. 2003, AJ, 126, 815

Lee, Y.-W., Gim, H. B., & Casetti-Dinescu, D. I. 2007, ApJ, 661, L49

Lee, Y.-W., Joo, J.-M., Sohn, Y.-J., et al. 1999, Nature, 402, 55

Leon, S., Meylan, G., & Combes, F. 2000, A&A, 359, 907

Mackey, A. D., & Gilmore. G. F. 2004, MNRAS, 355, 504

Majewski, S. R., Skrutskie, M. F., Weinberg, M. D., & Ostheimer, J. C. 2003, ApJ, 599, 1082

Martin, N. F., Ibata, R. A., Bellazzini, M., et al. 2004, MNRAS, 348, 12

Martínez-Delgado, D., Butler, D. J., Rix, H.-W., et al. 2005, ApJ, 633, 205

Martínez-Delgado, D., Gómez-Flechoso, M. Á, Aparicio, A., & Carrera, R. 2004, ApJ, 601, 242

McLaughlin, D. E., & van der Marel, R. P. 2005, ApJS, 161, 304

McWilliam, A., & Rich, R. M. 1994, ApJS, 91, 749 Vicari, A. 2006, ApJ, 644, 940

Montuori, M., Capuzzo-Dolcetta, R., Di Matteo, P., Lepinette, A., & Miocchi, P. 2007, ApJ, 659, 1212

Moore, B., Diemand, J., Madau, P., Zemp, M., & Stadel, J. 2006, MNRAS, 368, 563

Moore, B., Ghigna, S., Governato, F., et al. 1999, ApJ, 524, L19

Nakasato, N. & Nomoto, K. 2003, ApJ, 588, 842

Newberg, H. J., Yanny, B., Grebel, E. K., et al. 2003, ApJ, 596, L191

Newberg, H. J., Yanny, B., Rockosi, C., et al. 2002, ApJ, 569, 245

Newberg, H. J., Yanny, B., & Willett, B. A. 2009, ApJ, 700, L61 ed. H. Morrison & A. Sarajedini (San Francisco: ASP), 14

Noyola, E., & Gebhardt, K. 2006, AJ, 132, 447

Odenkirchen, M., Grebel, E. K., Dehnen, W., et al. 2003, AJ, 126, 2385

Odenkirchen, M., Grebel, E. K., Kayser, A., Rix, H.-W., & Dehnen, W. 2009, AJ, 137, 3378

Odenkirchen, M., Grebel, E. K., Rockosi, C. M., et al. 2001, ApJ, 548, L165

Olszewski, E. W., Saha, A., Knezek, P., et al. 2009, AJ, 138, 157

Possenti, A., D'Amico, N., Manchester, R. N., et al. 2003, ApJ, 599, 475

Rocha-Pinto, H. J., Majewski, S. R., Skrutskie, M. F., Crane, J. D., & Patterson, R. J. 2004, ApJ, 615, 732

Rockosi, C. M., Odenkirchen, M., Grebel, E. K., et al. 2002, AJ, 124, 349

Schaerer, D., & Charbonnel, C. 2011, MNRAS, 413, 2297 2010, ApJ, 725, 1175

Schlegel, D. J., Finkbeiner, D. P., & Davis, M. 1998, ApJ, 500, 525

Searle, L., & Zinn, R. 1978, ApJ, 225, 357

Shin, J., Kim, S. S., & Takahashi, K. 2008, MNRAS, 386, L67

Sohn, Y.-J., Park, J.-H., Rey, S.-C., et al. 2003, AJ, 126, 803

Stetson, P. B. 1987, PASP, 99, 191

Stetson, P. B., & Harris, W. E. 1988, AJ, 96, 909

Testa, V., Zaggia, S. R., Andreon, S., et al. 2000, A&A, 356, 127

Trager, S. C., King, Ivan R., & Djorgovski, S. 1995, AJ, 109, 218

van den Bergh, S. 1993, ApJ, 411, 178

Vivas, A. K., Zinn, R., Andrews, P., et al. 2001, ApJ, 554, L33

Vivas, A. K., Jaffé, Y. L., Zinn, R., et al. 2008, AJ, 136, 1645

Vivas, A. K., & Zinn, R. 2006, AJ, 132, 714

Wilson, C. P. 1975, AJ, 80, 175

Yanny, B., Newberg, H. J., Grebel, E. K., et al. 2003, ApJ, 588, 824

Yanny, B., Newberg, H. J., Kent, S., et al. 2000, ApJ, 540, 825

Zoccali, M., Lecureur, A., Barbuy, B., et al. 2006, A&A, 457, L1

Zoccali, M., Renzini, A., Ortolani, S., et al. 2003, A&A, 399, 931

Zucker, D. B., Belokurov, V., Evans, N. W., et al. 2006, ApJ, 650, L41

This manuscript was prepared with the AAS LaTeX macros v5.2.

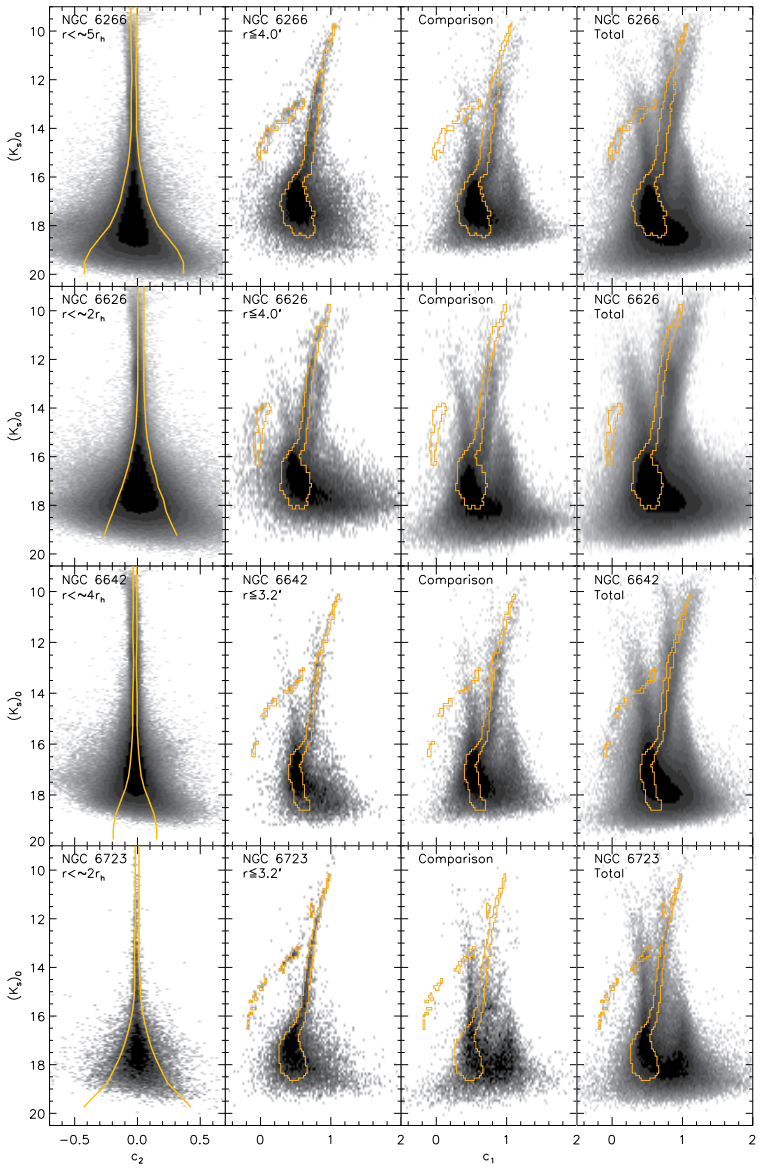

Fig. 1.— (c_2, K) and (c_1, K) color magnitude diagrams of stars for four globular clusters. The left panel shows the (c_2, K) CMD of stars in central region of clusters. The lines in the (c_2, K) plane are $2\sigma_{c_2}(K)$ rejecting limit at K magnitudes. The second, third and fourth panels are the (c_1, K) CMDs for the stars in the cluster central region, in the assigned comparison region, and in the total field of four clusters. The grid lines in (c_1, K) CMDs indicate the filtering mask envelope where the signal-to-noise ratios of cluster star counts are maximized through a C-M mask filtering technique. The stars outside the grid lines are highly unlikely to be cluster members. The optimal contrast filtering technique was also applied to this envelope.

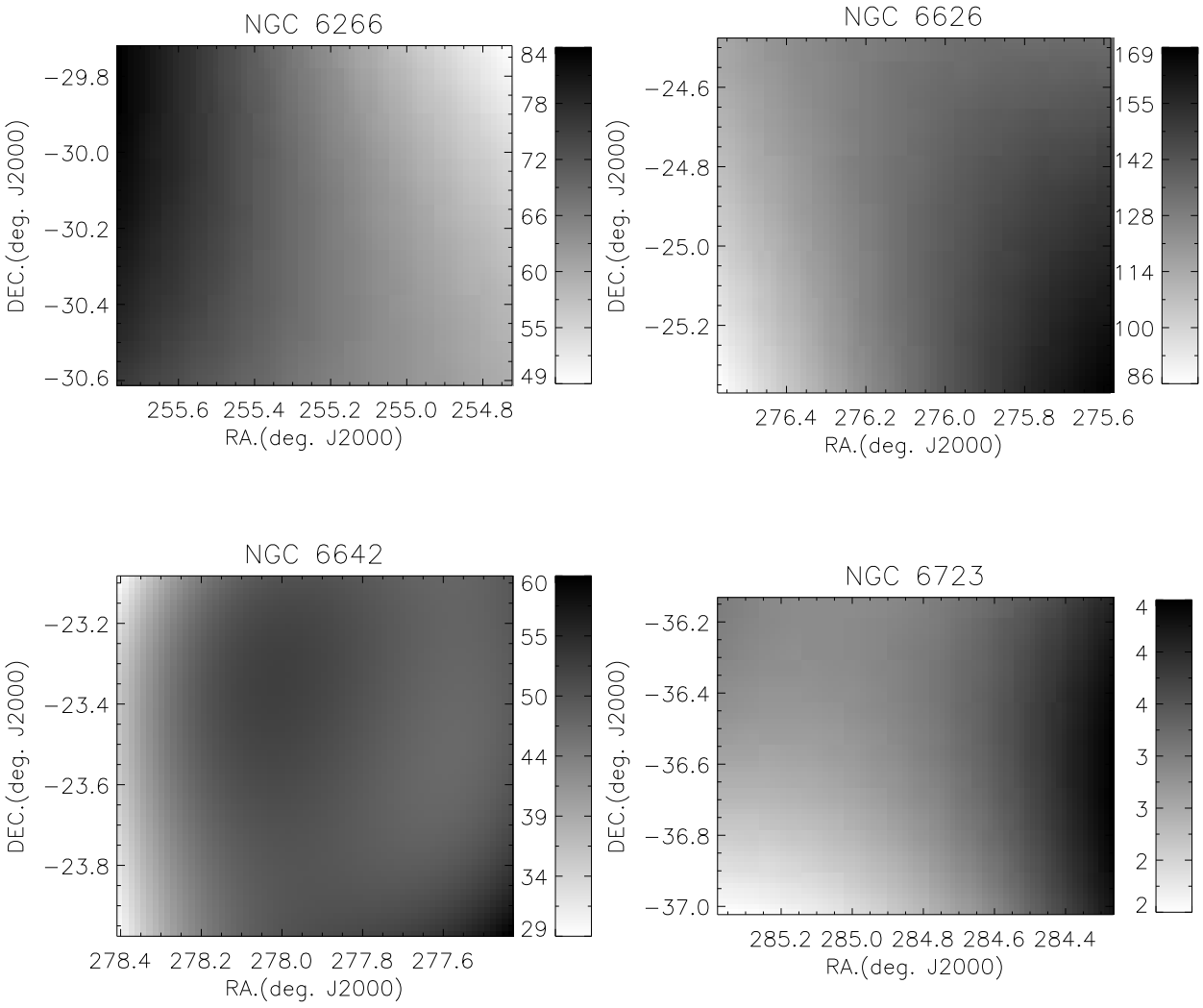

Fig. 2.— The field star contribution maps for four globular clusters. The density gradients and variation across the globular clusters were described with gray scale. The sidebar indicates the number of stars per square pixels.

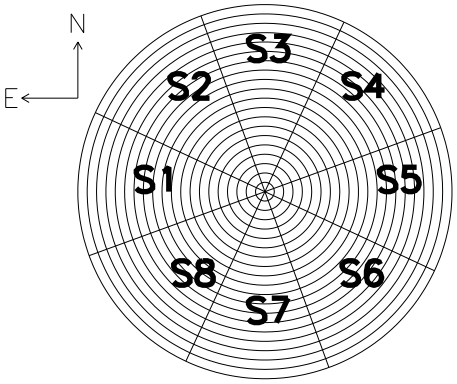

Fig. 3.— Reseau plot used for radial density profile. The radial surface densities were measured in concentric annuli. We divided each annulus into eight angular sections (S1-S8) in order to derive the surface density profiles in a different direction.

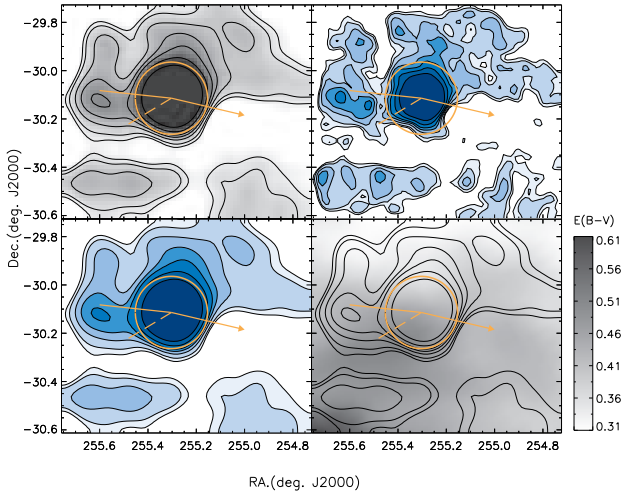

Fig. 4.— From top-left to bottom-right, the star count map around NGC 6266, the surface density maps smoothed by Gaussian kernel values of 0°.045 and 0°.12, overlaid with iso-density contour levels $0.5\sigma, 1.0\sigma, 2.0\sigma, 3.0\sigma, 4.0\sigma, 6.0\sigma$ and 10.0σ, and the distribution map of E(B-V). The circle indicates a tidal radius of NGC 6266. The arrow represent the proper motion of cluster. Solid line indicates the direction of the Galactic center, and dashed line shows the perpendicular direction of the Galactic plane.

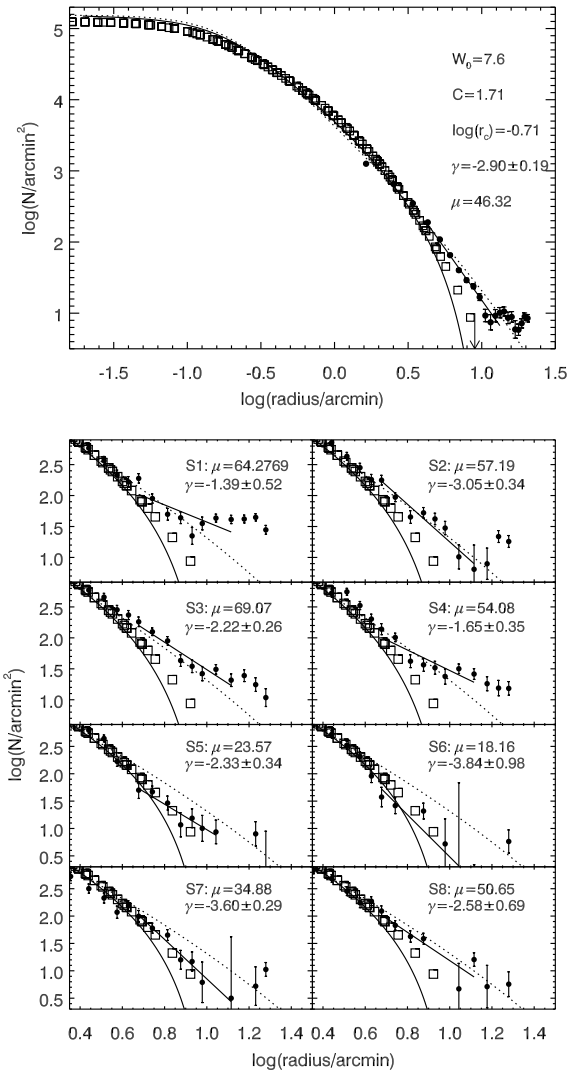

Fig. 5.— *Upper* : Radial surface density profile of NGC 6266 with a theoretical King model (solid curve) and Wilson model (dotted curve). In central region, we plot surface brightness profile (Trager et al. 1995) as open squares. The arrow indicates the tidal radius ($r_t = 8'.97$) of NGC 6266. The overdensity feature at the region of $\sim 0.5r_t \leq r \leq\sim 1.5r_t$ was described by a power-law, i.e., a straight line in logarithmic scale with a slope of $\gamma = -2.90 \pm 0.19$. The mean number density of stars in the overdensity region is estimated as $\mu = 46.32$ per arcminute square. *Lower* : Radial surface density profiles of eight different angular sections (S1∼S8). The other notations are the same as those of the radial surface density profile in the upper panel.

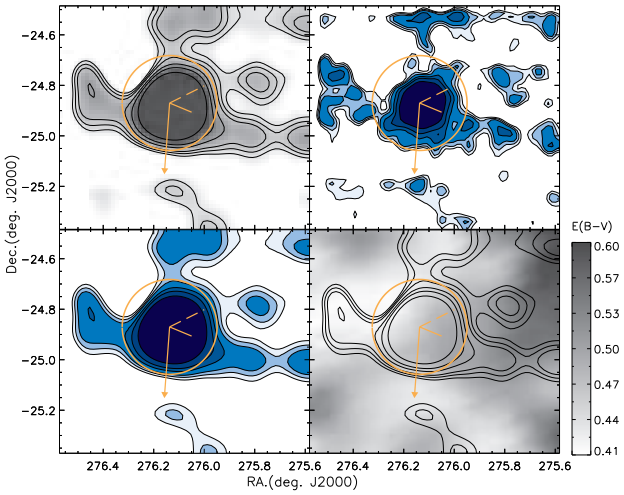

Fig. 6.— The star count map around NGC 6626, surface density contour maps smoothed by Gaussian kernel values of 0°.045 and 0°.12, and distribution map of E(B-V) of Schlegel et al. (1998) were plotted from top-left to bottom-right panel. The contour levels indicate $1.0\sigma, 1.5\sigma, 2.0\sigma, 3.0\sigma, 4.0\sigma$, and 6.0σ. The long arrow indicated the proper motion of cluster. The different lines indicate the direction of the Galactic center(solid line) and the perpendicular direction of the Galactic plane(dashed line). The circle indicates a tidal radius of NGC 6626.

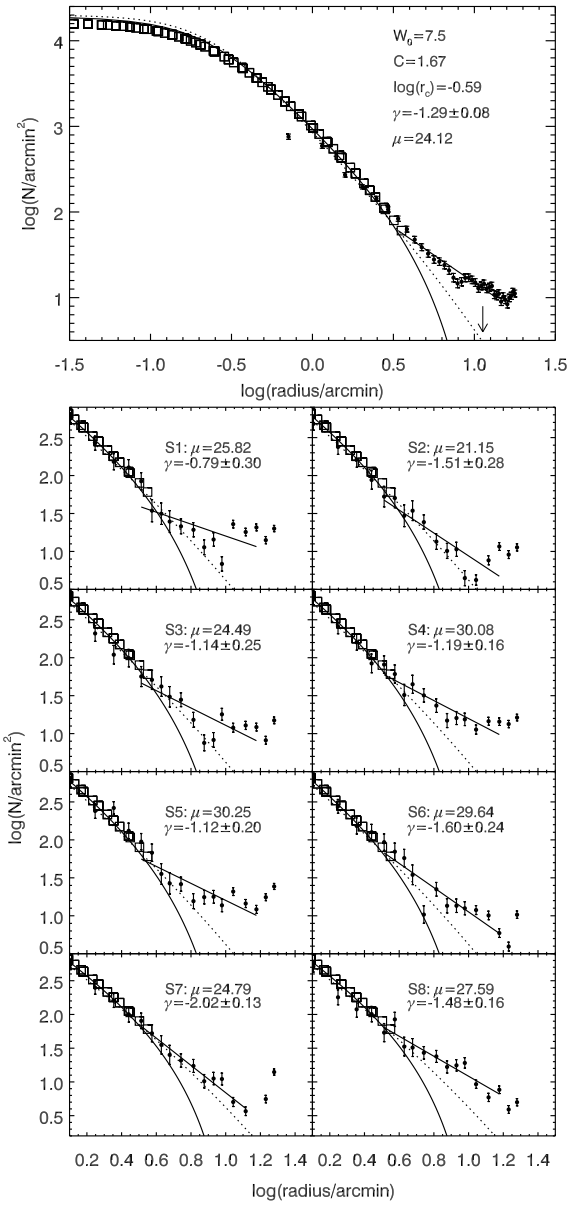

Fig. 7.— *Upper* : Radial surface density profile of NGC 6626 with a King model (solid curve) and a Wilson model (dotted curve). The profile within the detected overdensity region, $\sim 0.28r_t \leq r \leq \sim 1.5r_t$, is represented by a power-law, i.e., a dotted straight line in logarithmic scale with a slope of $\gamma = -1.29 \pm 0.08$. The mean number density of stars in the overdensity region is estimated as $\mu = 24.12$ per arcminute square. *Lower* : Radial surface density profiles in eight different angular sections (S1∼S8). For clarity, we magnified the radial profile of the overdensity feature. The other notations are the same as those of the radial surface density profile in the upper panel.

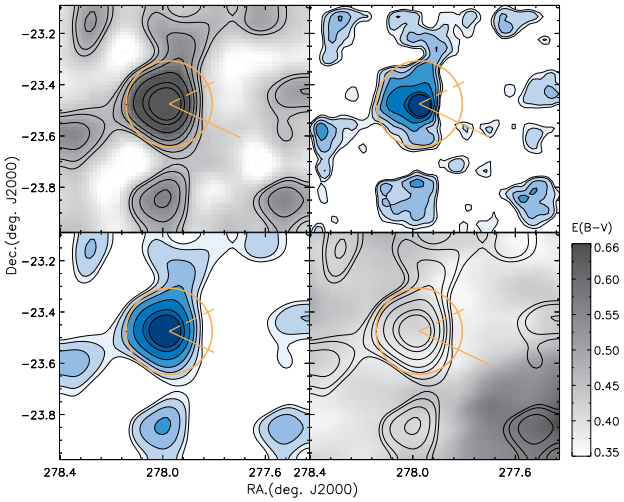

Fig. 8.— From top-left to bottom-right, the star count map around NGC 6642, the surface density maps smoothed by different Gaussian kernel values, and the E(B-V) extinction map around the cluster. The Gaussian kernel values are 0°.045 and 0°.12. Isodensity contour levels are $0.5\sigma, 1.0\sigma, 2.0\sigma, 3.0\sigma, 5.0\sigma, 8.0\sigma$, and 10.0σ. The circle indicates a tidal radius of NGC 6642. Solid line indicates the direction of the Galactic center, and dashed line shows the perpendicular direction of the Galactic plane.

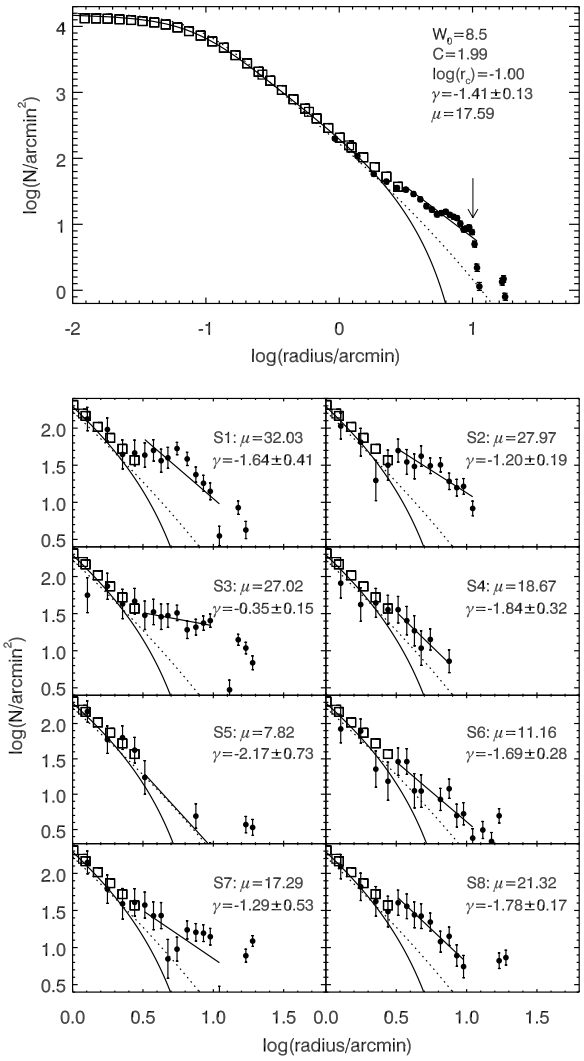

Fig. 9.— *Upper* : Radial surface density profile of NGC 6642 with a King model (solid curve) and a Wilson model (dotted line) There is overdensity feature at $\sim 0.3r_t \leq r \leq\sim 1.5r_t$, which is represented by a power-law, i.e., a dotted straight line in logarithmic scale with a slope of $\gamma = -1.41 \pm 0.13$. The mean number density of stars in the overdensity region is estimated as $\mu = 17.59$ per arcminute square. *Lower* : Radial surface density profiles of eight different angular sections (S1∼S8). The radial density points, which were calculated by interpolation from neighbor densities, were indicated by open triangle. The other notations are the same as those of the radial surface density profile in the upper panel.

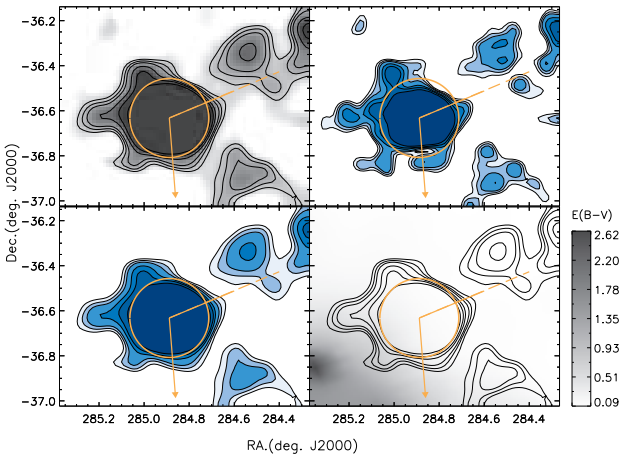

Fig. 10.— From top-left to bottom-right panels, the star count map around NGC 6723, the surface density maps smoothed by Gaussian kernel values of 0°.07 and 0°.11, the distribution map of E(B-V). Isodensity contour levels are $2.0\sigma, 2.5\sigma, 3.0\sigma, 4.0\sigma, 5.0\sigma$, and 7.0σ. The circle indicates a tidal radius of NGC 6723. The arrow represent the proper motion of cluster. Solid line indicates the direction of the Galactic center, and dashed line shows the perpendicular direction of the Galactic plane. We note that the direction to the Galactic center and the Galactic plane almost coincide, thus two lines overlap each other.

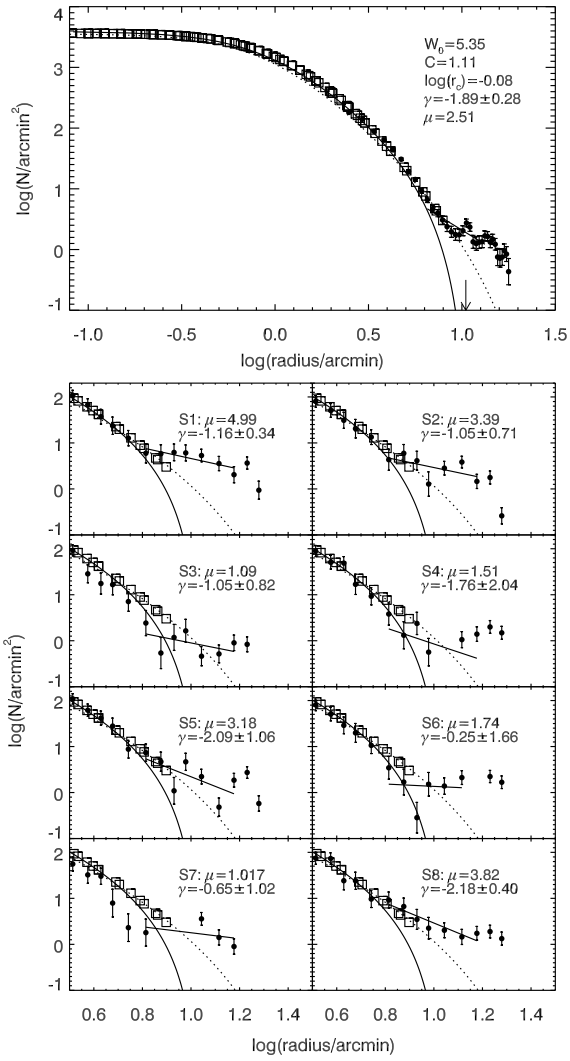

Fig. 11.— *Upper* : Radial surface density profile of NGC 6723 with a King model (solid line) and a Wilson model (dotted line). The overdensity feature appears at the region of $\sim 0.6r_t \leq r \leq \sim 1.5r_t$. The overdensity feature are represented by a power-law, i.e., a dotted straight line in logarithmic scale with a slope of $\gamma = -1.89 \pm 0.28$. The mean number density of stars in the overdensity region is estimated as $\mu = 2.51$ per arcminute square. *Lower* : Radial surface density profiles of eight different angular sections (S1∼S8). For clarity, we magnified the radial profile of the overdensity feature. The other notations are the same as those of the radial surface density profile in the upper panel.

Table 1. Basic parameter for four target globular clusters and position of three comparison fields

Target	α (J2000)	δ (J2000)	R_{sun} (kpc)	R_{GC} (kpc)	r_c ($'$)	r_t ($'$)	[Fe/H]	Index
NGC 6266	17:01:12.80	-30:06:49.4	6.8	1.7	0.22	8.97	–1.18	-
NGC 6626	18:24:32.81	-24:52:11.2	5.5	2.7	0.24	11.27	–1.32	-
NGC 6642	18:31:54.10	-23:28:30.7	8.1	1.7	0.1	10.07	–1.26	-
NGC 6723	18:59:33.15	-36:37:56.1	8.7	2.6	0.83	10.51	–1.10	-
Comparison1	18:31:37.44	-29:19:30.36	-	-	-	-	-	NGC 6266, NGC 6642
Comparison2	17:12:59.28	-23:12:51.84	-	-	-	-	-	NGC 6626
Comparison3	19:09:22.32	-32:55:42.96	-	-	-	-	-	NGC 6723

Note. — R_{sun} and R_{GC} are distances from the Sun and the Galactic center, respectively. r_c and r_t indicate the core radius and tidal radius. The basic parameter information is from the catalogue Harris 1996 (2010 edition). Index indicates the globular clusters to which comparison fields applied in C-M mask filtering and optimal contrast filtering technique.

Table 2. Observation Summary of four globular clusters

Target	Filter	Exp. time (micro-step × dither × second)	FWHM ($''$)
NGC 6266	J	$4 \times 5 \times 1s, 4 \times 5 \times 5s$	0.78, 0.77
	H	$4 \times 5 \times 1s, 4 \times 5 \times 5s$	0.78, 0.76
	K	$4 \times 5 \times 1s, 4 \times 5 \times 10s$	0.74, 0.77
NGC 6626	J	$4 \times 5 \times 1s, 4 \times 5 \times 5s$	0.92, 0.90
	H	$4 \times 5 \times 1s, 4 \times 5 \times 5s$	0.88, 1.05
	K	$4 \times 5 \times 1s, 4 \times 5 \times 10s$	0.91, 0.76
NGC 6642	J	$4 \times 5 \times 1s, 4 \times 5 \times 5s$	0.86, 0.87
	H	$4 \times 5 \times 1s, 4 \times 5 \times 5s$	0.81, 0.79
	K	$4 \times 5 \times 1s, 4 \times 5 \times 10s$	0.82, 0.78
NGC 6723	J	$4 \times 5 \times 1s, 4 \times 5 \times 5s$	0.95, 0.99
	H	$4 \times 5 \times 1s, 4 \times 5 \times 5s$	1.07, 1.06
	K	$4 \times 5 \times 1s, 4 \times 5 \times 10s$	0.98, 0.97

Table 3. The coefficient a and b of new color indices for each cluster

Target	a	b
NGC 6266	0.748	0.663
NGC 6626	0.784	0.621
NGC 6642	0.757	0.653
NGC 6723	0.750	0.661